WATER CAPTURE

Evolution of water structures in metal-organic frameworks for improved atmospheric water harvesting

Nikita Hanikel[1], Xiaokun Pei[1], Saumil Chheda[2], Hao Lyu[1], WooSeok Jeong[3], Joachim Sauer[4]*, Laura Gagliardi[5]*, Omar M. Yaghi[1]*

Although the positions of water guests in porous crystals can be identified, determination of their filling sequence remains challenging. We deciphered the water-filling mechanism for the state-of-the-art water-harvesting metal-organic framework MOF-303 by performing an extensive series of single-crystal x-ray diffraction measurements and density functional theory calculations. The first water molecules strongly bind to the polar organic linkers; they are followed by additional water molecules forming isolated clusters, then chains of clusters, and finally a water network. This evolution of water structures led us to modify the pores by the multivariate approach, thereby precisely modulating the binding strength of the first water molecules and deliberately shaping the water uptake behavior. This resulted in higher water productivity, as well as tunability of regeneration temperature and enthalpy, without compromising capacity and stability.

The recent discovery that porous metal-organic frameworks (MOFs) (1, 2) can extract atmospheric water in the desert to produce potable water (3–7) raises the question of how such MOFs "pluck out" water from arid air and easily release it, especially on the molecular level. Indeed, the evolution of water structures in MOFs and synthetic crystals is sought after, but a full mechanistic understanding of water uptake behavior is still missing (8–17). Although the water positions in some of these structures have been determined with diffraction techniques (11, 13, 16), the mechanism of how water-binding sites are populated is much harder to decipher because it requires high-quality data and the ability to collect these data at each loading increment. Knowledge of the mechanism for water behavior in MOFs should enable the design of water-harvesting systems that can operate with greater energy efficiency and productivity.

We successfully determined the uptake mechanism of MOF-303 {[Al(OH)(PZDC)], where PZDC^{2-} = 1-H-pyrazole-3,5-dicarboxylate}, the state-of-the-art water-harvesting MOF (Fig. 1A)

(5, 6), by using single-crystal x-ray diffraction (SCXRD) to locate all of the water molecules in its pores and identify the molecule-by-molecule sequence of filling these locations. Previously, the inorganic units of MOFs were observed as the strongest water-binding sites (10, 11, 15, 18). Using experimental and computational methods, we found that the polar organic linkers play a primary role as adsorptive sites in MOF-303, where they are aligned to create hydrophilic pockets into which the first water molecules bind strongly and seed further uptake.

We used the multivariate MOF strategy (19, 20), in which multiple functionalities line the pores across the crystal, to achieve accurate design of the geometry and strength of water interactions in a series of nine multivariate MOFs. This approach allowed us to precisely control the relative humidity (RH) levels at which these compounds extract water from arid air, as well as heat of adsorption, desorption temperature, and water productivity, without compromising the pore size, shape, or hydrolytic stability of the MOFs. On a fundamental level, this study transforms the development of water-harvesting materials from a trial-and-error activity to precision molecular design and deliberate shaping of the water behavior in the pores.

The structure of MOF-303 is based on infinite rod-like secondary building units (SBUs) consisting of alternating cis-trans corner-shared AlO$_6$ octahedra that are connected by PZDC^{2-} linkers (Fig. 1). Topological reconstruction of this MOF provides the **xhh** topology (text S2). This arrangement has neighboring pyrazole functionalities that point toward each other and form a pocket defined by three μ$_2$-OH groups and two N(H) on each of the linkers (Fig. 1, A and B). Water adsorption into this environment resulted in an unusual water sorption isotherm in which the isotherm exhibits a small but functionally impacting step (labeled S; red segment in Fig. 1A) at low vapor pressures. Step S reduced the water-harvesting output per cycle (working capacity) for this MOF by about 20 wt%, and upon cycling extensively, this reduction would amount to large quantities of water. As additional water

[1]Department of Chemistry and Kavli Energy Nanoscience Institute, University of California, Berkeley, CA 94720, USA. [2]Department of Chemical Engineering and Materials Science, Chemical Theory Center, and Minnesota Supercomputing Institute, University of Minnesota, Minneapolis, MN 55455, USA. [3]Department of Chemistry, Chemical Theory Center, and Minnesota Supercomputing Institute, University of Minnesota, Minneapolis, MN 55455, USA. [4]Institut für Chemie, Humboldt-Universität zu Berlin, 10099 Berlin, Germany. [5]Department of Chemistry, Pritzker School of Molecular Engineering, James Franck Institute, and Chicago Center for Theoretical Chemistry, University of Chicago, Chicago, IL 60637, USA.

*Corresponding author. Email: js@chemie.hu-berlin.de (J.S.); lgagliardi@uchicago.edu (L.G.); yaghi@berkeley.edu (O.M.Y.)

Fig. 1. Water sorption isotherm and crystal structure of MOF-303. (A) Water sorption isotherm at 25°C, where P is water vapor pressure and P_{sat} is the saturation water vapor pressure. The water uptake is displayed gravimetrically and with respect to the asymmetric unit [Al(OH)(PZDC)]$_2$ of MOF-303. The three segments of the isotherm are highlighted in red, yellow, and blue in the background. The linker 1H-3,5-pyrazoledicarboxalic acid (H$_2$PZDC) and MOF crystal structure are shown in the inset. The initial step is labeled with S. (B) Side view visualizing two hydrophilic pockets defined by a pair of pyrazole-based linkers with their nitrogen atoms pointing toward each other and flanked by two aluminum oxide rod-like SBUs. Here and in other figures, coordinate systems are given for guidance. Al, blue polyhedron; O, pink; C and H, gray; N, green.

molecules filled the pore, a large water uptake within a small RH window was observed in the isotherm (yellow segment in Fig. 1A). Further water uptake by MOF-303 filled the pores entirely over a large RH range (blue segment in Fig. 1A). We sought to learn how to eliminate the initial step S by understanding the water uptake process through location of the adsorption sites and the mechanism with which they are populated.

Accordingly, we grew single crystals of sufficient size (15 µm × 15 µm × 20 µm; text S1) to be studied by synchrotron SCXRD. For the determination of the water structures at different loadings, we developed a procedure by which it was possible to slowly desorb water upon gradually ramping up the temperature of the dry protective gas stream. The process was designed to be sufficiently mild to avoid crystal cracking, which has often prevented SCXRD analysis. This procedure initiated a controlled release of water molecules from the MOF pores, which we monitored closely by collecting a series of SCXRD datasets, each acquired in a time frame of 3 to 12 min (text S3). The almost perfect overlay of the adsorption and desorption isotherm curves with minimal hysteresis observed for MOF-303 (Fig. 1A) indicated that the water sorption process

was reversible and could be studied in either the adsorption or desorption mode. Thus, our SCXRD measurements allowed us to decipher the molecular water adsorption mechanism of MOF-303.

The SCXRD analysis revealed that the first and strongest water adsorption site of the framework (labeled I) was located between the pyrazoles, in which the water molecule formed three hydrogen bonds (H-bonds) to two pyrazole groups and one μ_2-OH group, with respective distances of 2.797(7) Å, 2.887(9) Å, and 2.798(6) Å between the heteroatoms (Fig. 2A). The second water molecule (II) was also situated between the pyrazoles and formed two H-bonds with N∶O$_{water}$ distances of 2.72(2) Å and 2.96(3) Å (Fig. 2B). Both of these sites were located within the hydrophilic pocket of MOF-303 and could be associated with the step S at low vapor pressures.

The next water molecule occupied site III and only interacted with the remaining μ_2-OH group at a distance of 2.89(3) Å (Fig. 2C). The fourth water molecule (IV) H-bonded to the water molecules at I and II but not to the framework, thus forming a trimeric cluster (I, II, and IV; Fig. 2D), with the water molecule at III remaining detached from it. At this loading stage, such clusters were isolated from others

in neighboring symmetry equivalent pockets (Fig. 2E). Adsorption of water molecules at I to IV represented the seeding stage (red segment in Fig. 1A), which served as a nucleus for binding of other water molecules.

Using density functional theory (DFT) calculations (text S4), we predicted the seeding water adsorption sites in MOF-303. We found that the first adsorbed water molecule exhibited two short H-bonds to the pyrazole moieties (both 2.8 Å) and one short H-bond to the μ_2-OH group (2.7 Å), similar to our experimental observations. The second water molecule was determined to be H-bonded to the neighboring pyrazole pair (2.6 and 2.8 Å) and confirmed the role of the aligned pyrazole functionalities as primary adsorption sites. The third and fourth water molecules H-bonded to the second μ_2-OH group and to the initially adsorbed water molecules, respectively. This geometrical water arrangement closely resembled the obtained SCXRD structures, where the first three molecules adsorbed onto the framework and the fourth molecule H-bonded with these molecules. Furthermore, by applying a many-body decomposition scheme (text S4), we calculated the individual binding energy contributions of each water molecule at the seeding stage. A clear trend between H-bonding interaction
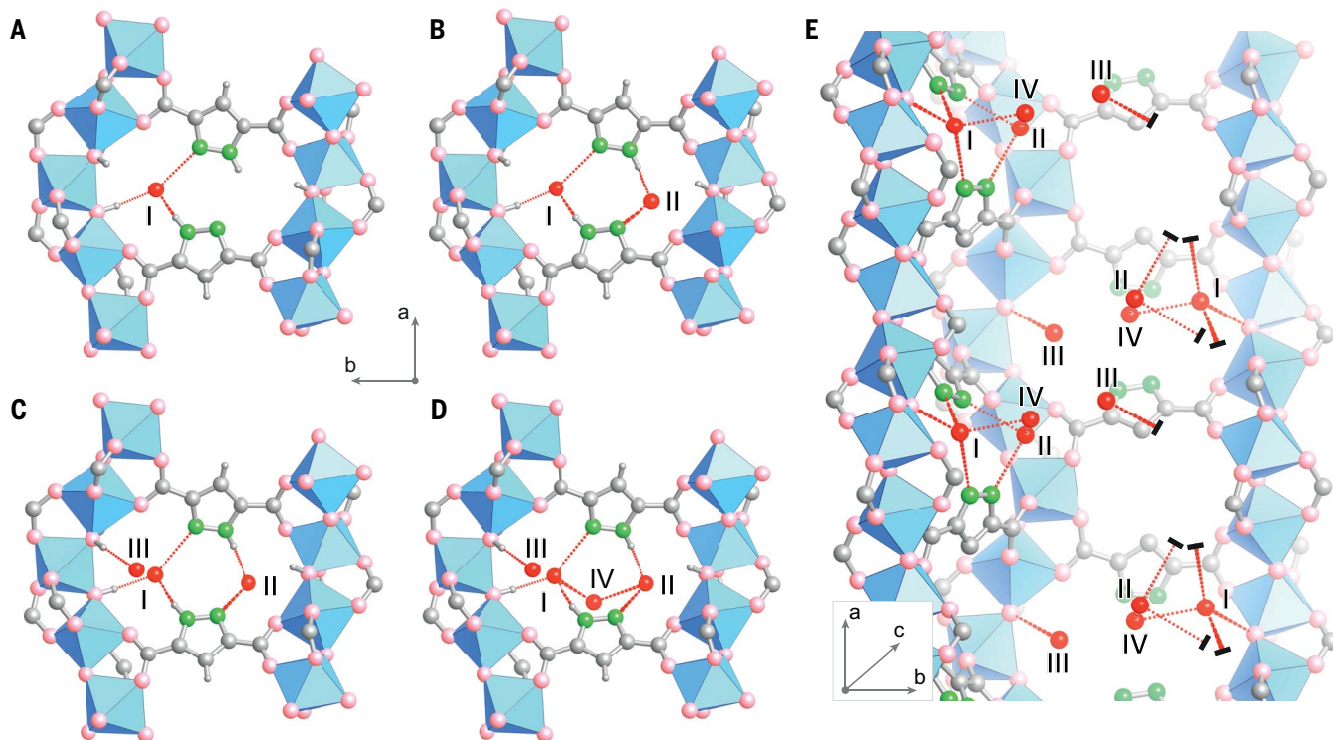
Fig. 2. Crystal structures of the seeding water adsorption sites in MOF-303. (**A** to **D**) Sequential adsorption of the first four water molecules (I to IV) per asymmetric building unit depicted in the hydrophilic pocket, as determined by SCXRD analysis. (**E**) Three-dimensional view of the first four water molecules in the framework pore. Shown crystallographic snapshots were captured at 0.04 g g^{-1} in (A), 0.06 g g^{-1} in (B), 0.11 g g^{-1} in (C), and 0.15 g g^{-1} in (D) and (E). H-bonds are depicted as red dashed lines. Black solid bars at the end of H-bonds in (E) represent binding interactions to the MOF, which is partially omitted for clarity. Al, blue polyhedron; O in the framework structure, pink; O in H$_2$O, red; C and H, gray; N, green. H atoms in (E) are omitted for clarity.

energies with the framework and the water-filling sequence was observed, thus further confirming the preferential siting of water molecules in MOF-303.

The crystallographic study revealed that additionally adsorbing water molecules filled the pores by interacting with other water molecules rather than with the framework itself (Fig. 3). Adsorption of two additional water molecules at V and VI yielded a structure in which the neighboring clusters (I, II, and IV) were connected with each other through new

H$_2$O in different water structure evolution stages: ● Seeding ● Clustering ● Networking
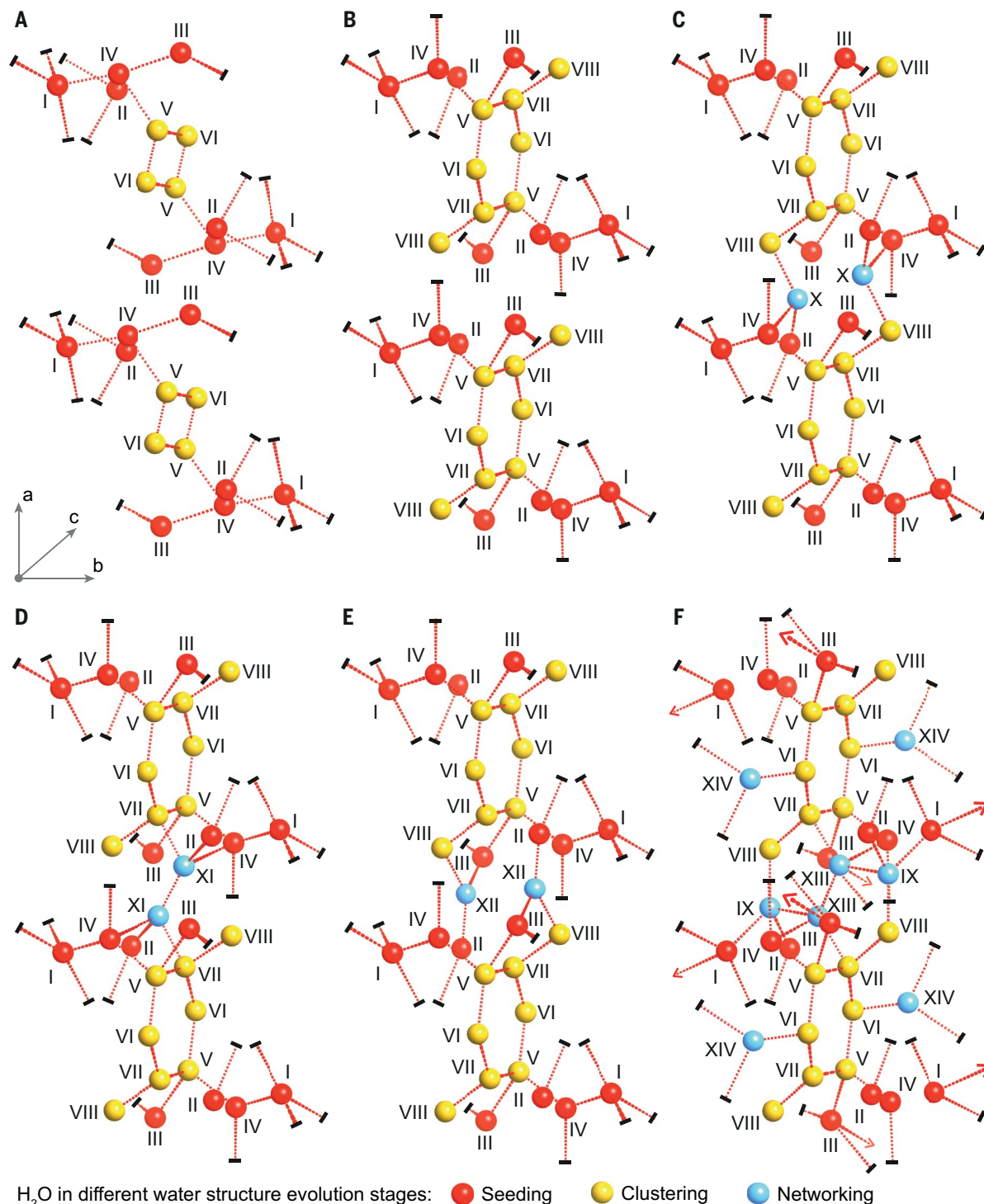
Fig. 3. Evolution of water structures in MOF-303 at increased loadings.
(**A** to **F**) Water molecule positions at different adsorption states, as determined by SCXRD analysis. The water structures in (C) to (F) were consecutively co-populated and are depicted separately for clarity. Shown crystallographic snapshots were captured at 0.18 g g^{-1} in (A), 0.36 g g^{-1} in (B), 0.40 g g^{-1} in (C), 0.41 g g^{-1} in (D), 0.42 g g^{-1} in (E), and 0.45 g g^{-1} in (F). H-bonds are depicted as red dashed lines. Black solid bars at the end of H-bonds represent binding interactions to the MOF, which is omitted for clarity. The viewing direction for all panels is the same as in Fig. 2E. Arrows in (F) indicate periodic extension of water chains into a three-dimensional water network. Only the O atoms in H$_2$O are displayed, with colors indicating the pore-filling stages: seeding, red; clustering, yellow; networking, blue.

water tetramer clusters (Fig. 3A). Upon addition of water molecules at VII and VIII, the tetramers transformed into hexamers (V to VII) with one dangling water molecule at VIII connected to VII (Fig. 3B). The evolution of water structures from V to VIII, termed the clustering stage, fell in the yellow segment of the water sorption isotherm (Fig. 1A).

At higher water loadings, the sequential partial filling of sites IX to XIV together with the fully occupied sites I to VIII created infinite H-bonded water chains of clustering units (networking stage; blue segment in Fig. 1A). First, the mutually exclusive, disordered sites IX and X were populated simultaneously, with the associated water molecules H-bonding to the water molecules at II, IV, and VIII (Fig. 3C; only X is depicted for clarity). Second, site XI, which was connected to II, IV, and VII, was partly filled (Fig. 3D). Third, partial population of site XII connected II, III, and VIII (Fig. 3E). At the highest loading, the pyrazole functionalities became slightly displaced, whereas a water molecule inserted at XIII between sites IV, VII, and IX, consequently rearranging the water molecule at IX to H-bond to the species at I, II, and VIII.

These changes to the framework and restructuring of the water network resulted in partial filling of site XIV, in which the water molecule H-bonded to the O-atoms of the carboxy functional groups (Fig. 3F). At this loading, sites IX to XIV were co-populated and partly filled, and the occupational factors of these sites summed up to two water molecules in total (table S3). Ultimately, neighboring chain networks connected into a three-dimensional water network. The highest water load of 10 water molecules per asymmetric unit, whose crystallographic locations were presented above, corresponded to a total uptake of 0.45 g g^{-1} and was in agreement with the total uptake found in the water sorption isotherm (Fig. 1A).

Our series of SCXRD measurements allowed us to further elaborate the impact of water uptake on the framework. Throughout the water adsorption process, the MOF underwent substantial structural transformations and the unit cell parameter changes were tracked at different loadings (table S1). At its extreme, the MOF lattice changed from 14.5037(6) Å to 16.7259(7) Å in the b direction, and from 101.465(2)° to 105.091(2)° in β. We also conducted SCXRD measurements on the fully activated MOF at both 330 and 100 K and observed only incremental unit cell changes on the order of 0.01 Å. This result confirmed that these transitions were not caused by temperature variations but rather by water filling the pores.

In contrast, a larger difference was observed in the unit cell dimensions (up to 0.5 Å in the b direction) between the activated and fully loaded MOF at 100 K. Close examination of

the hydrophilic pocket at different loadings revealed that the neighboring pyrazoles underwent adjustments to fit the water molecules (table S5). Specifically, the closest intermolecular N ꞉ N distance in the activated structure was 3.218(5) Å. Then, upon first and second water binding, this distance grew to 3.708(7) Å and 3.760(8) Å, respectively, as the pyrazole functionalities moved apart to accommodate the water molecules. At full water loading, the N ꞉ N distance peaked at 4.364(3) Å and allowed the formation of a three-dimensional water network. Complementary DFT calculations indicated an increase in framework strain at higher water loadings, which was, however, compensated by favorable H-bond interactions (text S4).

Having identified both experimentally and computationally that the step in the water sorption isotherm originated from water interactions with two neighboring pyrazole functionalities (sites I and II), we decided to control the H-bonding in the pocket by substituting PZDC^{2-} with another linker that was less hydrophilic. We used 2,4-furandicarboxylic acid (H$_2$FDC) to synthesize a new MOF, MOF-333 {[Al(OH)(FDC)], where FDC^{2-} = 2,4-furandicarboxylate; Fig. 4A}, isoreticular to MOF-303 (21, 22); that is, its rod-like SBUs consisted of cis-trans corner-shared AlO$_6$ octahedra. The sequence of the SBU was likely programmed by the similar angle between the carboxylic acid groups of the two linkers (158° for H$_2$PZDC and 156.5° for H$_2$FDC, as evidenced by SCXRD; text S3) and resulted in higher pore volumes, and consequently higher water uptakes, relative to other Al-MOFs built from rod-like SBUs (23).

In comparison to pyrazole, we expected furan to undergo weaker H-bonding with water molecules because it is less acidic and less basic, which is a consequence of the absence of acidic H atoms and the lower protonation propensity of the more electronegative O atom. Indeed, DFT calculations of the adsorption structures in MOF-333 suggested a stronger interaction of the water molecules with the µ$_2$-OH group rather than the linker molecule, which was reflected in their respective interatomic distances (text S4). Furthermore, the computed binding energies indicated that water adsorption into the MOF-303 pocket was substantially stronger than into the MOF-333 pocket.

By following a SCXRD procedure similar to that described above for MOF-303, we identified the primary adsorption sites in MOF-333 (text S3). The initially bound two water molecules (I′ and II′) could be distinguished by SCXRD analysis. They exhibited one strong H-bond to an individual µ$_2$-OH group with O$_{OH}$ ꞉ O$_{water}$ distances of 2.770(14) Å and 2.779(15) Å. In addition, water molecule I′ had only a very weak interaction with the furan linker with an O$_{furan}$ ꞉ O$_{water}$ distance

of 3.01(2) Å, thus further confirming that this linker choice moderated the water sorption properties of MOF-303 (Fig. 4A).

Next, we conducted a water sorption analysis on MOF-333 and observed an ideally shaped water sorption isotherm with a steep step at 22% RH and without the step S observed for MOF-303 (Fig. 4A). This value set a low RH cutoff at which our new MOF could operate. To extend its working range to more arid conditions, we prepared a series of multivariate MOFs consisting of both PZDC^{2-} and FDC^{2-}. The nine synthesized MOFs covered the entire range of linker mixing ratios, including the two single-linker frameworks MOF-303 and MOF-333. We use the nomenclature 'n/m,' which describes the input ratio of PZDC^{2-} to FDC^{2-} (n to m); for example, '5/3' denotes a 5-to-3 input ratio of PZDC^{2-} to FDC^{2-} and '0/8' refers to the single-linker MOF-333.

Powder x-ray diffraction (PXRD) analysis revealed that all nine products were isostructural (text S5). The linker ratio for each MOF in the multivariate series, determined by nuclear magnetic resonance (NMR) analysis on completely base-hydrolyzed MOF crystals and elemental microanalysis, was nearly proportional to the input ratio (Fig. 4B and text S6). The close correspondence between the input and output ratios and the reproducible nature of this reaction chemistry indicated a robust reaction across all ratios—a behavior that may be called formulaic. Additionally, the presence and homogeneous distribution of PZDC^{2-} in the multivariate MOF crystals and the absence of single-linker MOFs were verified by scanning electron microscopy coupled with energy-dispersive x-ray spectroscopy (text S7). Mapping of Al, C, N, and O showed homogeneous elemental distribution within the crystal outlines, and the overall intensity of the N signal continuously decreased with increasing substitution of PZDC^{2-} by FDC^{2-} (fig. S34).

The thermal stability and porosity of our products were assessed by thermogravimetric analysis and N$_2$ sorption analysis, respectively. The MOF series exhibited no weight loss up to 375°C under N$_2$ and up to 325°C under air (text S8). The BET areas (1280 to 1360 m^2 g^{-1}), pore volumes (0.48 to 0.51 cm^3 g^{-1}), and diameters (~9.4 Å) extracted from N$_2$ sorption measurements on all nine compounds were comparable and consistent with an isostructural series of MOFs (text S9). The small variation in pore volumes stands in contrast to the conventional method of tuning MOF hydrophilicity involving the addition of functional groups to the framework backbone, which invariably reduces the free pore volume and subsequently the water uptake capacity (11, 24, 25).

We observed that the substitution of PZDC^{2-} with increasing amounts of FDC^{2-} continuously shifted the water isotherm step toward
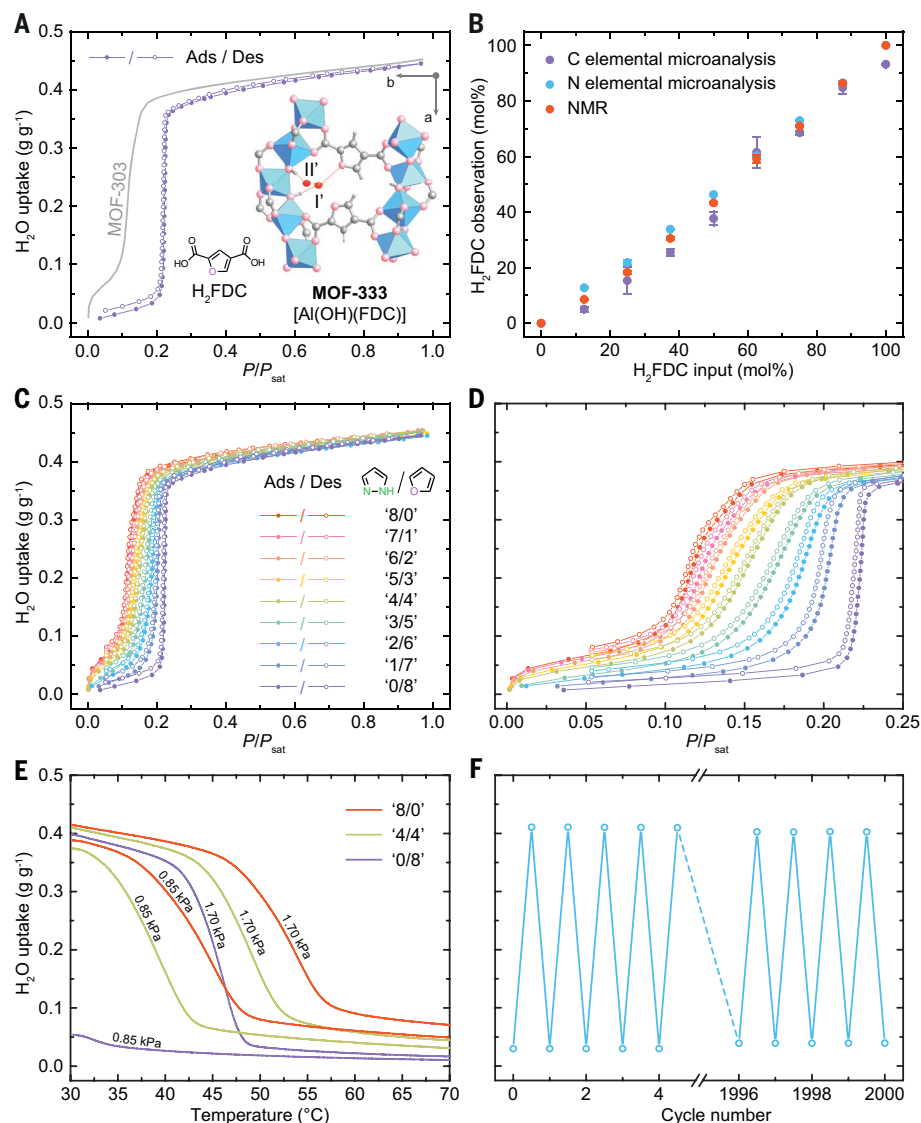
Fig. 4. Characterization of the multivariate MOF series. (**A**) Water sorption isotherm of MOF-333 at 25°C. The water sorption isotherm of MOF-303 is shown as a gray line for reference. The linker 2,4-furandicarboxylic acid (H_2FDC) and the pocket of MOF-333 with the first two adsorption sites (I' and II') are shown in the inset. Al, blue polyhedron; O in the framework structure, pink; O in H_2O, red; C and H, gray. For simplicity, only one orientation of the C/O positional disorder of FDC^{2-} in the MOF structure is shown. (**B**) H_2FDC linker ratios determined by NMR and C/N elemental microanalysis are plotted against the respective input linker ratios. Standard deviations (estimated from duplicate measurements on the same sample for elemental microanalysis and analysis of three separate samples for NMR) are depicted as error bars. (**C** and **D**) Full-range and low-pressure region of the water sorption analyses on the multivariate MOF series at 25°C. (**E**) Water vapor isobar measurements at 0.85 to 1.70 kPa for '8/0,' '4/4,' and '0/8.' (**F**) Water adsorption–desorption cycling of '4/4' between 30° and 85°C at 1.70 kPa for 2000 cycles of ~75 min each.

higher vapor pressures and covered the entire range between the water sorption isotherms of MOF-303 and MOF-333 (Fig. 4C). Furthermore, in accord with the analogous pore volumes of all MOF compounds, the maximal water uptake capacity was not compromised upon linker substitution. The initial step in the isotherm of MOF-303 was successfully mitigated with increasing $PZDC^{2-}$ substitution

and its prominence disappeared at FDC^{2-} contents > 50%. All multivariate MOFs exhibited negligible hysteresis between the adsorption and desorption curves (Fig. 4D). This feature is desirable because hysteresis tends to reduce the working capacity and generally increases the energetic requirement for sorbent regeneration. The formulaic character of this multivariate series (Fig. 4B) and the continuous

variation of the water sorption behavior allowed us to accurately design water sorption isotherms by simply choosing an appropriate input linker ratio.

Additionally, we assessed the impact of the multivariate strategy on the water adsorption enthalpies by extending our water sorption analysis to other temperatures (15°, 35°, and 45°C). Similar to the measurements at 25°C, the water sorption isotherms exhibited continuity within the multivariate series, lack of hysteresis, and similar maximal uptakes, which indicated consistent performance across different temperatures (text S10). From these isotherms, we estimated the differential adsorption enthalpy Δh_{ads} for all nine compounds using the Clausius-Clapeyron equation (text S10). With an increasing degree of FDC^{2-} incorporation, the average Δh_{ads} increased continuously from –53 to –50 kJ mol^{-1}. We note that the heat of condensation of water at 25°C is –44 kJ mol^{-1} and indicates the maximal possible enthalpy value for Δh_{ads}. Thus, the multivariate method allowed us to effectively decrease the adsorption heat penalty by up to 35%.

Moreover, our approach could be used to design water sorbents with ultralow desorption temperatures, as demonstrated with isobaric desorption curves at water vapor pressures between 0.85 and 1.70 kPa (corresponding to 20 to 40% RH at 30°C) for '8/0,' '4/4,' and '0/8' (text S10). The isobars exhibited a steep step that increased with higher vapor pressures. Notably, the minimal desorption temperature could be decreased up to 10°C by substituting $PZDC^{2-}$ with FDC^{2-} in the MOF structure (Fig. 4E). Furthermore, and in accordance with the isotherms, the working capacity increased with higher FDC^{2-} contents up to 15%. Both of these factors have a fundamental impact on energetic requirements and output per cycle of a water-harvesting system. Additionally, higher desorption temperatures restrict the number of cycles the water harvester can perform daily because longer heating and subsequent cooling times will be necessary to drive the higher temperature gradients.

Finally, we confirmed that mixing of $PZDC^{2-}$ and FDC^{2-} within one MOF crystal does not compromise the hydrolytic stability of the single-linker framework by exposing '4/4' to a water vapor pressure of 1.7 kPa and cycling the temperature between 30° and 85°C (Fig. 4F and text S10)—a test that reliably verifies the MOF's longevity (7, 26). After 2000 uptake and release cycles, the sorbent retained ~97% of its working capacity.

REFERENCES AND NOTES

1. O. M. Yaghi, M. J. Kalmutzki, C. S. Diercks, *Introduction to Reticular Chemistry: Metal-Organic Frameworks and Covalent Organic Frameworks* (Wiley-VCH, 2019).
2. L. Öhrström, F. M. Amombo Noa, *Metal-Organic Frameworks* (American Chemical Society, 2021).
3. H. Kim *et al.*, *Science* **356**, 430–434 (2017).

4. H. Kim *et al.*, *Nat. Commun.* **9**, 1191 (2018).
5. F. Fathieh *et al.*, *Sci. Adv.* **4**, eaat3198 (2018).
6. N. Hanikel *et al.*, *ACS Cent. Sci.* **5**, 1699–1706 (2019).
7. N. Hanikel, M. S. Prévot, O. M. Yaghi, *Nat. Nanotechnol.* **15**, 348–355 (2020).
8. A. I. Kolesnikov *et al.*, *Phys. Rev. Lett.* **93**, 035503 (2004).
9. X. Lin *et al.*, *J. Am. Chem. Soc.* **128**, 10745–10753 (2006).
10. Y.-K. Seo *et al.*, *Adv. Mater.* **24**, 806–810 (2012).
11. H. Furukawa *et al.*, *J. Am. Chem. Soc.* **136**, 4369–4381 (2014).
12. J. Varlec *et al.*, *New J. Chem.* **40**, 4178–4186 (2016).
13. S. M. Towsif Abtab *et al.*, *Chem* **4**, 94–105 (2018).
14. M. Wahiduzzaman, D. Lenzen, G. Maurin, N. Stock, M. T. Wharmby, *Eur. J. Inorg. Chem.* **2018**, 3626–3632 (2018).
15. A. J. Rieth, K. M. Hunter, M. Dincă, F. Paesani, *Nat. Commun.* **10**, 4771 (2019).
16. V. Bon *et al.*, *J. Mater. Chem. A* **7**, 12681–12690 (2019).
17. N. C. Burtch *et al.*, *Nat. Chem.* **12**, 186–192 (2020).
18. D. F. Sava *et al.*, *Chem. Mater.* **25**, 2591–2596 (2013).
19. H. Deng *et al.*, *Science* **327**, 846–850 (2010).
20. L. M. Aguirre-Díaz *et al.*, *J. Am. Chem. Soc.* **137**, 6132–6135 (2015).
21. M. Eddaoudi *et al.*, *Science* **295**, 469–472 (2002).
22. V. Colombo *et al.*, *J. Am. Chem. Soc.* **134**, 12830–12843 (2012).
23. X. Liu, X. Wang, F. Kapteijn, *Chem. Rev.* **120**, 8303–8377 (2020).
24. H. Reinsch *et al.*, *Chem. Mater.* **25**, 17–26 (2013).
25. N. Ko *et al.*, *J. Mater. Chem. A* **3**, 2057–2064 (2015).
26. J. E. Mondloch *et al.*, *Chem. Commun.* **50**, 8944–8946 (2014).
27. N. Hanikel *et al.*, Computational results for the publication "Evolution of water structures in metal-organic frameworks for improved atmospheric water harvesting". Zenodo (2021); https://doi.org/10.5281/zenodo.5294977.

Science

Evolution of water structures in metal-organic frameworks for improved atmospheric water harvesting

Nikita HanikelXiaokun PeiSaumil ChhedaHao LyuWooSeok JeongJoachim SauerLaura GagliardiOmar M. Yaghi

Designing water uptake

Although the locations of water molecules in some porous materials have been determined with diffraction techniques, determining the filling sequence of water sites has been challenging. Hanikel *et al.* used single-crystal x-ray diffraction to locate all of the water molecules in pores of the metal-organic framework MOF-303 at different water loadings (see the Perspective by Öhrström and Amombo Noa). They used this information on the water molecule adsorption sequence to modify the linkers of this MOF and control the water-harvesting properties from humid air for different temperature regimes. —PDS

View the article online
https://www.science.org/doi/10.1126/science.abj0890
Permissions
https://www.science.org/help/reprints-and-permissions

Use of think article is subject to the Terms of service